SCIENCE CHINA
Physics, Mechanics & Astronomy

• Article •

May 2026 Vol. 69 No. 5: 250311
https://doi.org/10.1007/s11433-025-2816-7

Realization of quantum data assimilation for a two-dimensional quasi-geostrophic model based on a coherent Ising machine

Yu-Xuan Jia[1,2†], Wei Zhong[1†*], Wei You[3], Hua-Dong Du[1], Neng-Fei Gong[2], Yan-Chen Jiang[2], Yao Yao[1], Yi-Xing Cao[3,4], Li-Xin Yuan[5], Yin Ma[5], Kai Wen[5], and Tie-Jun Wang[2*]

[1] *College of Advanced Interdisciplinary Studies, National University of Defense Technology, Changsha 410073, China*
[2] *School of Physical Science and Technology, Beijing University of Posts and Telecommunications, Beijing 100876, China*
[3] *College of Atmospheric Sciences, National University of Defense Technology, Changsha 410073, China*
[4] *Fundamental Education Department, Army Engineering University of PLA, Nanjing 211101, China*
[5] *Beijing QBoson Quantum Technology Co., Ltd., Beijing 100015, China*

Received July 8, 2025; accepted September 22, 2025; published online March 26, 2026

Data assimilation (DA), vital for numerical weather prediction and Earth system modeling, struggles with escalating computational demands from complex environmental datasets. We introduce a quantum-inspired DA (QDA) framework using coherent Ising machines (CIMs): an optical solver based on the quantum squeezing effect, specialized in solving combinatorial optimization problems. The QDA method overcomes qubit limitations with domain decomposition and reformulates a classical three-dimensional variational assimilation (3D-VAR) into a quadratic unconstrained binary optimization (QUBO) problem mapped to an optical Ising Hamiltonian. Validated on a 512D quasi-geostrophic model, numerically simulated QDA achieves lower root mean square error than the classical method after 120 assimilation cycles. Single-assimilation cycle optical experiments show that QDA operates at 9.5% (25.31 ms) of the classical 3D-VAR runtime (266.4 ms), yielding a 10.5× speedup while maintaining accuracy. This demonstrates the potential of CIMs to revolutionize high-resolution environmental forecasting through energy-efficient, real-time assimilation, bridging quantum photonics and geophysics.

data assimilation, coherent Ising machine, quantum data assimilation

Citation: Y.-X. Jia, W. Zhong, W. You, H.-D. Du, N.-F. Gong, Y.-C. Jiang, Y. Yao, Y.-X. Cao, L.-X. Yuan, Y. Ma, K. Wen, and T.-J. Wang, Realization of quantum data assimilation for a two-dimensional quasi-geostrophic model based on a coherent Ising machine, Sci. China-Phys. Mech. Astron. **69**, 250311 (2026), https://doi.org/10.1007/s11433-025-2816-7

1 Introduction

The remarkable advancement of numerical weather prediction (NWP) in the late twentieth century stems from three pivotal innovations: physical process parameterization, ensemble forecasting, and data assimilation (DA), with DA—particularly 3D-VAR and 4D-VAR methods [1-3]—playing a central role in refining initial conditions by merging previous forecasts and observations into optimal spatiotemporal analysis fields [1]. Rooted in optimal estimation theory, DA minimizes error variance but faces NP-hard (non-deterministic polynomial-time hard) challenges, which belong to a class of problems that lack efficient exact solutions under classical computational models. These difficulties arise from its combinatorial complexity and large-scale computation dimensions. Especially in applicational numerical models like Weather Research and Forecasting,

†Equally contributed to this work
*Corresponding authors (Wei Zhong, email: zhongwei@nudt.edu.cn; Tie-Jun Wang, email: wangtiejun@bupt.edu.cn)

covariance matrices can reach 10^{14} elements, straining traditional Von Neumann architectures. Leading meteorological centers (e.g., European Centre for Medium-Range Weather Forecasts (ECMWF), National Oceanic and Atmospheric Administration, Japan Meteorological Agency (JMA)) rely on iterative variational DA methods, yet these consume disproportionate resources. ECMWF's 4DVAR uses 13.3% of total computation time—double that of a 10-day forecast—while JMA's DA demands 25 times more resources than forecasting itself, highlighting critical inefficiencies and significant data hurdles in modern NWP systems [4].

Beyond gradient-based optimization, DA can leverage alternative approaches such as simulated annealing (SA), a mathematical optimization method inspired by the physical annealing process designed to solve combinatorial optimization problems, and quantum annealing (QA), which exploits quantum systems to solve combinatorial optimization problems. In 2023, Kotsuki et al. [4] introduced a QA-driven DA scheme, simplifying the nonlinear loss function of 4DVAR into a quadratic unconstrained optimization problem (L-QUO). Testing on a 40-variable 1D Lorenz model, their experiments revealed the efficiency of QA: the D-Wave quantum annealer completed iterations in 0.028 s—over 4.5 times faster than classical methods (0.129 s) and twice as fast as simulated QA (0.057 s). Meanwhile, it still maintained comparable accuracy with root mean squared error (RMSE) as follows: classical 0.2109, simulated QA 0.2105, and QA 0.2209. However, QA faces practical constraints, including extreme operational environments (near absolute zero) and limited qubit connectivity. For example, the D-Wave Advantage 4.1 system contains 5627 physical qubits but only 177 usable logical qubits due to mapping challenges [4]. Even newer systems with more than 7000 physical qubits remain insufficient for large-scale optimization [5], as the available number of logical qubits lags far behind real-world DA requirements. These limitations underscore the need for breakthroughs in qubit scalability, error correction, and connectivity to unlock QA's potential for operational meteorology.

The coherent Ising machine (CIM) [6-11], an optical quantum computing system based on the Ising model [12], solves combinatorial optimization problems at room temperature, unlike quantum annealers that require near absolute zero conditions. Capable of handling 10^3-10^5 variables with linear scaling computation time, CIM has demonstrated efficiency in large-scale computation tasks, such as solving 100000 node maximum cut problems in milliseconds [10], and a maximum independent set problem with a scale of up to 40000 bits [13] within an 8-bit coupling resolution. The binary encoding of the QA-driven DA scheme [14] minimizes bits (requiring $\log_2 d$ bits per variable) but is suboptimal for quantum annealing due to noise sensitivity [15], which degrades precision. In contrast, the CIM, which leverages quantum compression effects at room temperature, resists quantum noise and employs a quantum parallel search to accelerate optimization [16]. This capability enables a CIM-based quantum data assimilation (QDA) method that overcomes DA computational bottlenecks, such as scalability and precision, and outperforms noise-prone quantum annealing systems.

Here, we report an application of QDA in a 32×16 grid 2D quasi-geostrophic (QG) model [17]. The quadratic cost function of 3DVAR can be encoded as a quadratic unconstrained binary optimization (QUBO) problem and transformed into an Ising Hamiltonian for employing CIM to solve the problem. To reduce quantum bit usage (from 5121 to 1401 or 1201, each field value is represented by 10 Ising variables for discretization), a domain decomposition method was introduced, dividing the whole grid into six overlapping subregions. The results of numerical simulation showed that the CIM-based QDA method can achieve comparable or lower RMSE in both the stream function field DA and the vorticity field DA over 120 assimilation cycles. A single-cycle DA experiment on CIM optical hardware (10-bit coupling resolution) demonstrated a solution time of 25.31 ms per DA-cycle (9.5% of the classical 3D-VAR methods (266.4 ms)) with competitive accuracy (the RMSE of QDA is 0.04436 and the RMSE of the classical methods is 0.04213). This highlights the potential of CIM for high-efficiency scalable DA in massive computing meteorological or oceanic models.

The structure of the paper is as follows: In sect. 2, QDA method and dimensionality reduction method are introduced. In sect. 3, QDA numerical simulation experiment results and optical CIM experiment results are introduced. Finally, a discussion and summary are given in sect. 4.

2 QDA method and dimensionality reduction method

2.1 Two-dimensional quasi-geostrophic model

The QG model is a simplified model that can be used to describe the core thermodynamic and dynamic processes of the atmospheric and oceanic systems. Since it retains the basic rotational characteristics of the systems, as well as the thermodynamic information related to the stratification of the fluid layers, it provides an effective theoretical framework for understanding the evolution laws and physical mechanisms of the atmospheric and oceanic systems [17-19]. In the field of DA algorithm research, the QG model is frequently used as a benchmark or test model due to its well-understood dynamical characteristics and the availability of mature numerical solving schemes [20-23]. We consider the following dimensionless QG model:

$$\begin{cases} \dfrac{\partial \omega}{\partial t} + \partial(\varphi, \omega) = 0, \\ \omega = \nabla^2 \varphi - F\varphi + f_0 + \dfrac{f_0}{H_0} h_s, \text{ in } \Omega \times [0, T], \\ \varphi \,|_{t=0} = \varphi_0, \end{cases} \quad (1)$$

where ω represents the potential vorticity, φ is the stream function, and $\partial(\varphi, \omega) = \varphi_x \omega_y - \varphi_y \omega_x$ is the horizontal nonlinear Jacobian operator, and $\nabla^2 = \partial^2/\partial x^2 + \partial^2/\partial y^2$ is the two-dimensional Laplacian operator. x and y are the eastward and northward coordinates, respectively, and t is time. F is the planetary Froude number, which measures the relative importance of vorticity stretching effects [24], f_0 is a representative parameter for the Coriolis term, H_0 is the vertical characteristic depth, and h_s is the topography.

For simplicity, the research object of this paper is a balanced atmospheric and oceanic system with large-scale and long-period characteristics. For this purpose, the initial field flow function φ_0 of a 32×16 grid region is constructed (see sect. 2), and its initial potential vortex distribution is obtained by inversion based on eq. (1) (see Figure 1(b)) to track the evolution of the thermal and dynamic characteristics of the atmospheric system. A numerical simulation of 120 DA cycles is performed for the fields of the stream function and potential vorticity of a QG model in a 32×16 grid region (totaling 720 evolution steps, corresponding to 119 h 50 min) to demonstrate the effectiveness of QDA. In order to address scalability challenges in CIM-based QDA for a 32×16 grid (which requiring at least 5121 Ising variables), we propose a domain decomposition method (see Method), and the whole 32×16 grid domain is partitioned into 6 overlapping subregions (four 14×10 grid subregions, two 12×10 grid subregions; the corresponding subregions without overlapping are indicated in white lines in Figure 1). The width of the overlapping part between adjacent subregions is four grid points.

2.2 Coherent Ising machine based on quantum compression effects

The N-spin Ising problem [25] is to find the configuration of spins $\sigma_i \in \{-1, +1\}$ that minimizes the energy function

$$H_{\mathrm{I}} = -\sum_{i<j}^{N} J_{ij}\sigma_i\sigma_j - \sum_{i}^{N} h_i\sigma_i, \quad (2)$$

where the particular problem instance being solved is specified by the $N \times N$ matrix $\mathbf{J}$. with elements J_{ij} and the N-length vector $\mathbf{h}$ with elements h_i. The CIM solves this combinatorial optimization using degenerate optical parametric oscillator (DOPO) networks. At room temperature, DOPO pulses adopt 0/π phases (spins ±1) through the quantum squeezing effect. For a CIM system with N DOPOs, its total photon decay rate is [26]

$$\Gamma = N - \sum_{1 \leqslant i<j \leqslant N}^{N} J_{ij}\sigma_i\sigma_j + \mathcal{O}\left(\frac{\epsilon^3 N^4}{(p-1)^3}\right), \quad (3)$$

where $\epsilon = \max|J_{ij}|$, and p is the pumping light intensity. Given a specific phase configuration $\{\sigma_i\}$ of DOPOs, the total photon decay rate of the CIM system corresponds exactly to the Ising Hamiltonian determined by J_{ij}, and the ground state of the Ising problem determines the oscillation threshold of the CIM system. As the pumping intensity increases, the lowest energy configuration of the Ising Hamiltonian is triggered first. By measuring the phase of the DOPO light

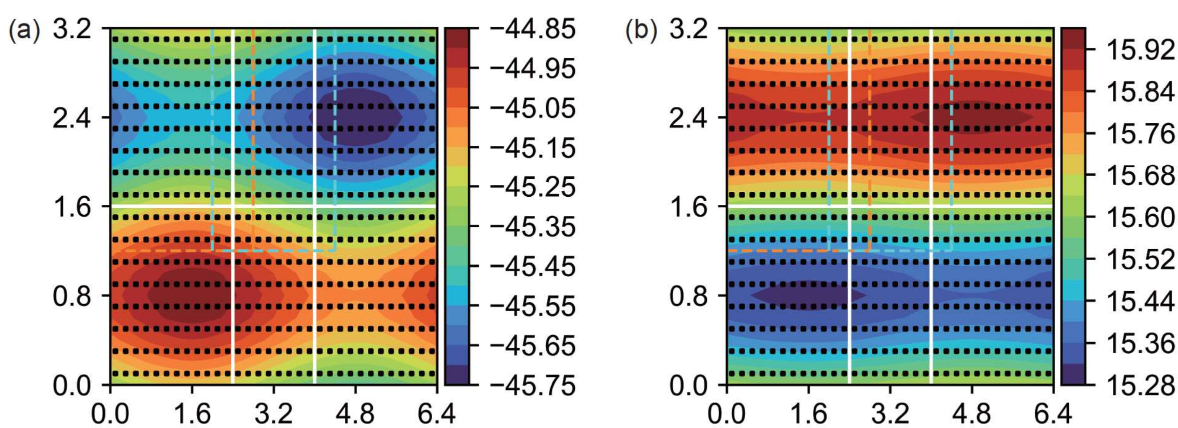

Figure 1 (Color online) Contour plots of the initial stream function field and initial potential vorticity field. The dimensionless calculation domain of the QG model is set to $\Omega = [0, 6.4] \times [0, 3.2]$. The corresponding dimensionless area size is [0, 6400 km]×[0, 3200 km]. The boundary conditions are double-periodic, and the discretization is performed with a 32×16 grid resolution, with mesh spacing $d = 0.2$ corresponding 200 km. Therefore, the dimension of QG model is 512. (a) Contour plot of the initial stream function field, with black solid points representing the grid point locations. The white solid lines indicate the division of subregions during the QDA. (b) Contour plot of the initial potential vorticity field, with the black solid points and white solid lines having the same meaning as in (a). The division of two adjacent overlapping subregions is shown in (b), with four overlapping grid points along boundaries of adjacent subregions.

pulses at this point, the ground-state solution of the Ising problem can be obtained, which is referred to as the minimum gain principle. This paper employs the numerically simulated CIM algorithm and the optical CIM device as two tools to solve DA problems.

2.3 QUBO modeling of the 3DVAR assimilation method and Ising model Hamiltonian

The 3DVAR assimilation method is based on the principle of optimal estimation, which organically combines the background field and the observation to form an analysis field with the minimum error variance. The cost function expression for the 3DVAR assimilation method [27] is given by

$$J(\mathbf{x}) = \frac{1}{2}(x-x_b)^{\mathrm{T}}\mathbf{B}^{-1}(x-x_b) + \frac{1}{2}(H(x)-y)^{\mathrm{T}}\mathbf{B}^{-1}(H(x)-y), \tag{4}$$

where $x \in \mathbb{R}^N$ represents the control variables of the assimilation system (e.g., potential vorticity or stream function), $x_b \in \mathbb{R}^N$ is the background field, $y \in \mathbb{R}^{n_{\mathrm{obs}}}$ is the observation. The matrix $\mathbf{B} \in \mathbb{R}^{N\times N}$ is the background error covariance, which contains prior information about model forecast errors, while $\mathbf{R} \in \mathbb{R}^{n_{\mathrm{obs}}\times n_{\mathrm{obs}}}$ is the observational error covariance matrix, related to the errors in the observational field, which is generally assumed to be a diagonal matrix. $H(x): \mathbb{R}^N \mapsto \mathbb{R}^{n_{\mathrm{obs}}}$ projects the model space onto the observational space, wherein $H(\cdot)$ denotes the observation operator. Our direct observation of the point establishes $H(\cdot)$ as a linear operator, defined by [28]

$$H(x) = \mathbf{H}x, \tag{5}$$

where $\mathbf{H} \in \mathbb{R}^{n_{\mathrm{obs}}\times N}$ is the observation matrix. N and n_{obs} are the dimensions of the model space and the observation space.

The classical 3DVAR method assimilates information from the background and observations by minimizing $J(x)$. The resulting analysis field x_a is defined as:

$$x_a = \mathrm{argmin} J(x). \tag{6}$$

In the following, we refer to the implementation of eq. (6) on a classical computer as the classical 3DVAR assimilation (CDA) method. Further, the algorithmic details of CDA are provided in Supplementary Material S1. While CDA is effective, its gradient-based optimization faces cubic complexity for large $\mathbf{B}$. To address this limitation, we introduce the QDA approach, whose complexity is linear for quadratic problems. In QDA, the cost function is reformulated in terms of the perturbation $\delta x = x - x_b$:

$$J(\delta x) = \frac{1}{2}\delta\mathbf{x}^{\mathrm{T}}(\mathbf{B}^{-1}+\mathbf{H}^{\mathrm{T}}\mathbf{R}^{-1}\mathbf{H})\delta x + (\mathbf{H}x_b - y)^{\mathrm{T}}\mathbf{B}^{-1}\mathbf{H}\delta x. \tag{7}$$

The continuous variable δx is discretized as:

$$\delta x = \alpha\mathbf{P}b, \tag{8}$$

where $b \in \{-1,1\}^{2NZ}$ is a binary vector encoding δx. The encoding matrix $\mathbf{P}$ is defined as:

$$\mathbf{P} = \mathbf{I}_N \otimes p, \tag{9}$$

with $\mathbf{I}_N$ the $N\times N$ identity matrix and

$$p = [-2^{Z-1},\ldots,-1,1,\ldots,2^{Z-1}]^{\mathrm{T}}, \tag{10}$$

where the integer precision parameter Z controls the resolution of the discretization. For each of the N dimensions of δx, the corresponding $2Z$ bits in b allow representation of $2^{Z+1}-1$ distinct values. For example, with $Z=5$, 10 bits encode 63 values in the range of $[-31\alpha, 31\alpha]$. The scalar α is a tunable precision scaling factor. In this work, we set $Z=5$.

This discretization scheme yields the QUBO Hamiltonian:

$$\begin{aligned} &H_Q(b) = \mathbf{b}^{\mathrm{T}}\mathbf{A}b + \mathbf{u}^{\mathrm{T}}b, \\ &\text{with } \mathbf{A} = \frac{\alpha^2}{2}\mathbf{P}^{\mathrm{T}}(\mathbf{B}^{-1}+\mathbf{H}^{\mathrm{T}}\mathbf{R}^{-1}\mathbf{H})\mathbf{P}, \\ &\mathbf{u}^{\mathrm{T}} = \alpha(\mathbf{H}x_b - y)^{\mathrm{T}}\mathbf{R}^{-1}\mathbf{H}\mathbf{P}. \end{aligned} \tag{11}$$

Converting b to Ising variables $\boldsymbol{\sigma} = 2b-1$ gives $H_{\mathrm{I}}(\boldsymbol{\sigma}) = \boldsymbol{\sigma}^{\mathrm{T}}\mathbf{Q}\boldsymbol{\sigma} + 2\mathbf{h}^{\mathrm{T}}\boldsymbol{\sigma}$, where $\mathbf{Q} = \mathbf{A}/4$ and $\mathbf{h}^{\mathrm{T}} = (\mathbf{1}^{\mathrm{T}}\mathbf{A} + \mathbf{u}^{\mathrm{T}})/4$. An auxiliary spin $\sigma_{2NZ+1} = 1$ embeds linear terms into $\mathbf{Q}' = \begin{bmatrix}\mathbf{Q} & \mathbf{h}\\ \mathbf{h}^{\mathrm{T}} & 0\end{bmatrix}$, yielding

$$H_{\mathrm{I}}(\sigma') = \sigma'^{\mathrm{T}}\mathbf{Q}'\sigma'. \tag{12}$$

Solving this Ising problem via CIM returns $x_a = \alpha\mathbf{P}b + x_b$.

2.4 QDA with domain decomposition and dimensionality reduction method

To address the scalability challenges in CIM-based QDA for a 32×16 grid—which requires 5121 Ising variables (512 dimensions with 10 bits per dimension plus one auxiliary bit)—we propose a domain decomposition method. The grid is partitioned into six non-overlapping subregions as shown in Figure 1 with white solid lines. For each subregion, a local background error covariance matrix $\mathbf{B}_i$ is extracted from the global matrix $\mathbf{B}$, allowing the original problem in eq. (12) to be reformulated into subregional Ising problems [29]:

$$H_{\mathrm{I}}(\boldsymbol{\sigma}') = \sum_i H_i(\boldsymbol{\sigma}'_i) - \frac{1}{2}\sum_{i<j} w_{ij}s_i s_j + \frac{1}{2}\sum_{i<j,\ uv} Q'_{iu,jv}, \tag{13}$$

where $H_i(\boldsymbol{\sigma}'_i)$ is the optimal Hamiltonian of the i-th subregion, and σ'_i denotes its corresponding optimal spin configuration. The coupling coefficient w_{ij} denotes the overall correlation between subregions and is derived from the quadratic matrix $\mathbf{Q}'$ through:

$$w_{ij} = \frac{1}{2}\sum_{v>u}\sigma'^{(u)}_i\sigma'^{(v)}_j Q'_{iu,jv}. \tag{14}$$

The Ising binary variable $s_i \in \{-1, 1\}$ represents a state label for each subregion i, and the second term in eq. (13) represents the impact of inter-subregion correlations on the global optimal solution. $Q'_{iu,jv}$ is an element from the full-area quadratic term matrix $\mathbf{Q}'$, which represents the relationship between the bit groups $\sigma'^{(u)}_i$ and $\sigma'^{(v)}_j$ where $\sigma'^{[u(v)]}_{i(j)}$ is the optimal Ising variable value for the $u(v)$-th grid point of the $i(j)$-th subregion. When the covariance between subregions is very small, the result of eq. (13) is primarily determined by the first and third terms. At this point,

$$H_{\mathrm{I}}(\boldsymbol{\sigma}') = \sum_i H_i(\boldsymbol{\sigma}'_i) + \frac{1}{2}\sum_{i<j,\ uv} Q'_{iu,jv}. \tag{15}$$

Eq. (15) enables the reformulation of the global optimization problem into six independent subregional problems under a non-overlapping partition. Once solved, the subregional solutions are merged back into the original global domain. However, in QDA, such a direct partition neglects the correlations across subregion boundaries, which may compromise solution quality near the boundaries and further introduce artificial discontinuities upon merging. To mitigate this issue, in practice we employ overlapping subregions with two grid width buffer zones, as illustrated by the dashed lines in Figure 1. This strategy allows boundary correlations to be preserved and ensures smoother transitions across adjacent subregions.

To efficiently implement this domain decomposition strategy, it is essential to know the spatial properties of the quadratic matrix $\mathbf{Q}'$. According to eqs. (7)-(12), the spatial characteristics of $\mathbf{Q}'$ are primarily determined by the background error covariance matrix $\mathbf{B}$. The spatial correlation structure of $\mathbf{B}$ directly influences the coupling strength between different grid points, which in turn determines the feasibility and accuracy of the proposed decomposition approach.

For the construction of $\mathbf{B}$, we adopt a distance-dependent Gaussian decay model [30] that reflects the physical nature of atmospheric error correlations. Here, $\mathbf{B}$ is decomposed as:

$$\mathbf{B} = \mathbf{D}(\mathbf{C}_X \otimes \mathbf{C}_Y)\mathbf{D}^{\mathrm{T}}, \tag{16}$$

where $\mathbf{C}_X$ and $\mathbf{C}_Y$ are correlation coefficient matrices in the x and y directions, respectively, and $\mathbf{D}$ is a diagonal matrix of error standard deviations. A separable Gaussian correlation model is adopted:

$$\mathbf{C}_X(x_i, x_j) = \mathrm{e}^{-\frac{(x_i - x_j)^2}{2L_x^2}}. \tag{17}$$

In the dimensionless QG system, the grid spacing is set to $d = 0.2$ (corresponding to 200 km). With $L_x = 0.2$ and $\mathbf{D} = \mathbf{I}_N$, the correlation coefficient between adjacent grid points ($\Delta x = L_x$) is approximately $\rho = 0.607$, while at a separation of three grid points ($\Delta x = 3L_x$), it decays to $\rho = 0.011$. This rapid decay of spatial correlation ($\rho < 0.011$ beyond $3L_x$) justifies domain decomposition with overlapping buffer zones to preserve boundary correlations, while safely neglecting interactions beyond this range, effectively reducing the number of Ising variables in localized assimilation.

By employing the overlapping domain decomposition method, the original 32×16 grid is divided into four 14×10 and two 12×10 subregions. After solving the subregional problems, the overlapping buffer zones are trimmed, and only the core non-overlapping values (data inside white solid lines in Figure 1) are retained. The processed subregional solutions are then merged back into the global domain, ensuring consistency across boundaries while avoiding redundancy from the overlaps. This strategy not only preserves boundary correlations but also significantly reduces computational demand, lowering the number of Ising variables from 5121 to 1401 and 1201 per subregion, respectively. Consequently, the method effectively improves the scalability of QDA under the constraint of limited spin bits. This approach shows potential in addressing scalability challenges under the constraint of limited spin bits.

2.5 Parameter and experiment setting

In this work, QDA is performed on stream function and potential vorticity fields in a 32×16 QG model (computational domain $\Omega = [0, 6.4] \times [0, 3.2]$) under periodic boundary conditions. The model employs Arakawa's energy-conserving scheme [31] and Adams-Bashforth time integration ($\Delta t = 0.006$, 10 min). The initial stream function fields φ_0 and the topography h_s are set to:

$$\varphi_0 = 0.1a\sin\left(\frac{2\pi x}{6.4}\right) + b\sin\left(\frac{2\pi y}{3.2}\right) + c,$$

$$h_s = 0.1\sin\left(\frac{2\pi x}{6.4}\right) + \sin\left(\frac{2\pi y}{3.2}\right) + 1,$$

where the initial field parameter is set to $a = 1.1853$, $b = 0.3259$, and $c = -45.3019$. The model parameters are set to $F = 1.012$, $f_0 = 10$, and $H = 10$. With these parameters defined, we focus on the balanced and stable atmospheric and oceanic fluid motion under wavy topography and periodic boundary conditions, which can remove the influence of external forcing and internal high-frequency perturbations on the evolution of atmospheric and oceanic fluids (as shown in Figure 1).

To enable scalable QDA implementation, the domain is first partitioned into six non-overlapping blocks (white solid lines in Figure 1). In each block, two additional grid points are then appended as a buffer along the boundaries, thereby transforming the non-overlapping blocks into overlapping subregions. With this decomposition, the number of required Ising variables is reduced to 1401 or 1201, compared to 5121 in the undivided case (with 10 Ising variables per field value). The Gaussian decaying background error covariance matrix **B** is modeled by eqs. (16) and (17) with correlation length parameters L_x=L_y=0.2, corresponding to 200 km. Under this setting, correlations between grid points separated by three or more grid intervals fall below 0.01, which we consider sufficiently small to be neglected.

The numerical experiments are conducted for 120 cycles (hourly updates, totaling 720 steps over 119 h 50 min). Both CDA and QDA are tested under full ($n_{\rm obs}$ = 512) and partial ($n_{\rm obs}$ = 128, 32, 8) observations with background noise σ_b = 0.05 and observation noise $\sigma_{\rm obs}$ = 0.005 (see sect. 3.1). These simulations are performed on an Intel i7-13700 CPU using Python 3.11.4 with NumPy and SciPy.

To further verify scalability and physical feasibility, QDA is also implemented on an optical CIM. The CIM platform used in this work features a 1 GHz pulsed laser, a 1 km fiber cavity, and a field-programmable gate array (FPGA)-based feedback system with 10-bit coupling resolution (−511 to 511 integers). Further details of the CIM are given in sect. 3.2. The optical experiment on a single assimilation cycle shows close RMSE values between simulator and physical machine, confirming the reliability of Ising-based solutions.

3 QDA experiment results

Many NWP centers have adopted rapid-update-cycling with 3DVAR to assimilate high-resolution observational data [32-35]. Building on this concept, we apply QDA in a similar rapid-update framework and evaluate its performance through two sets of experiments. Sect. 3.1 presents numerical simulations comparing QDA with CDA under both full and partial observation scenarios, while sect. 3.2 reports an experimental validation of QDA's computational efficiency using a CIM. Together, these results demonstrate the accuracy, scalability, and practical feasibility of QDA.

3.1 Numerical QDA simulations

Following the experimental configuration described in sect. 2.5, we conducted 120 DA cycles for the stream function and potential vorticity fields of the 32×16 QG model. Figure 2 presents a comparison of the stream function field contours from the true state, control run, and assimilation results (CDA and QDA) under full observation conditions. The true stream function field is generated by evolving the initial field φ_0 for 720 steps in the QG model. The initial background field, created by adding Gaussian noise $\mathcal{N}(0,\sigma_b^2\mathbf{I}_N)$ to φ_0, is similarly integrated to produce the control field (without

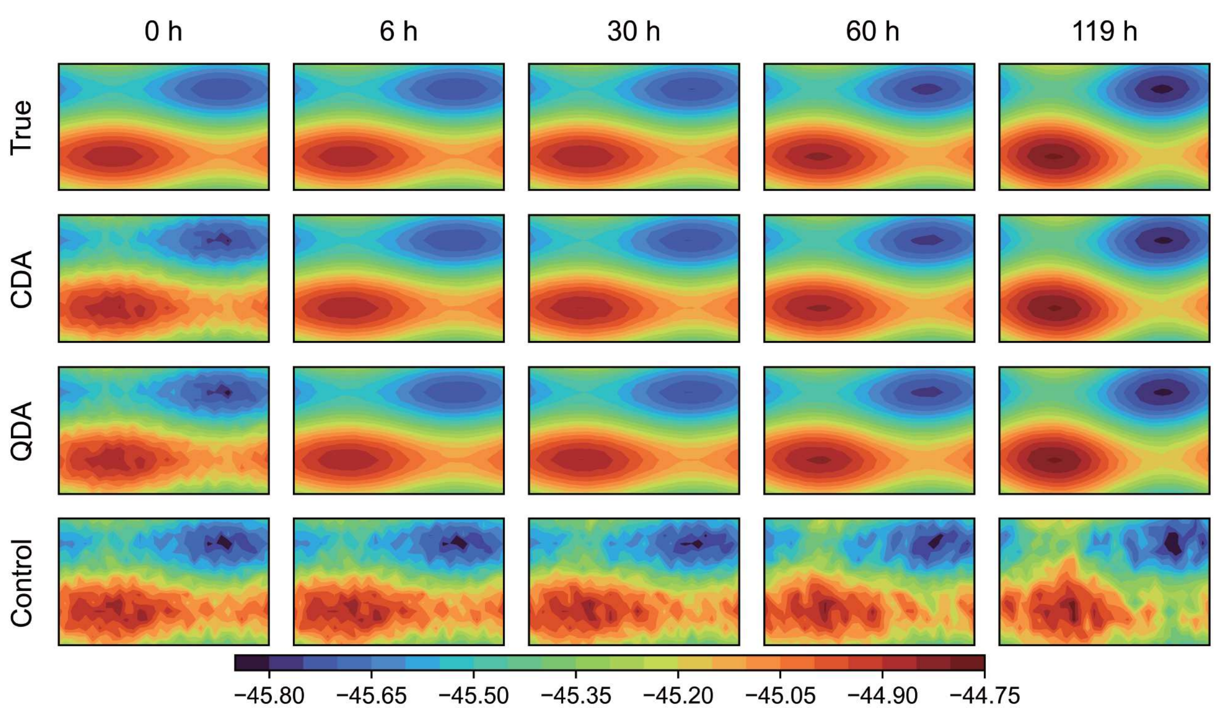

Figure 2 (Color online) Contour plots of the stream function field over time under full observation conditions. The figure illustrates the temporal evolution of different stream function fields, including both pure evolution and data assimilation effects. From top to bottom, the rows correspond to true field, CDA analysis field, QDA analysis field, and control field. The CDA and QDA fields are obtained through a rapid-update-cycling scheme, where 3D-Var is performed every six model integration steps over 120 cycles. QDA is implemented using a CIM simulator. The control field evolves purely through model dynamics without assimilation, serving as a baseline for error growth. The columns represent different time instances—0, 6, 30, 60, and 119 h—capturing the dynamic evolution of the system. By comparing the assimilated fields with the true field, one can assess the performance of different assimilation strategies in improving the stream function representation.

assimilation). The true and control fields serve as baseline fields for comparison. Assimilation begins at 0 h and proceeds hourly until 119 h, following a rapid-update-cycling approach. In each 1 h cycle, assimilation is performed at the beginning of the hour, and the resulting analysis field is used to forecast 6-time steps (each 10 min), which provide the background field for the next cycle. CDA and QDA methods share the same initial conditions as the control field, enabling direct evaluation of their assimilation performance. As shown in Figure 2, while the control field gradually diverges from the true state due to initial errors, both CDA and QDA analyses maintain a close approximation to the true field throughout the assimilation cycles and significantly reduce forecast errors. This demonstrates the effectiveness of both assimilation approaches. Similar results were observed for the vorticity fields DA in Figure 3. Here, initial potential vorticity fields derive from φ_0 via finite 5-point differences and over-relaxation iteration.

While Figures 2 and 3 show that QDA and CDA analysis fields are visually similar to the true state, further analysis is required to evaluate their relative performance. Here we evaluate the error by computing the RMSE of the analysis field with true field by

$$R(x) = \sqrt{\frac{(x-x_t)^{\mathrm{T}}(x-x_t)}{N}}, \tag{18}$$

where x_t denote the true fields, $N = 512$ is the number of grid points. In addition to the full observation case $n_{\mathrm{obs}} = 512$ (as shown in Figures 2 and 3), assimilation experiments were also conducted observation points are uniformly distributed over the computational domain. The under partial observation settings with $n_{\mathrm{obs}} = 128, 32, 8$. In all partial cases, the time series of RMSE for the stream function field during the rapid-update-cycling assimilation process is shown in Figure 4. Each assimilation cycle includes one analysis time step and six subsequent forecast steps (i.e., six RMSE values per cycle). In the full observation case, QDA outperformed CDA after 5 cycles ($R_{Q,S} = 0.00323$ vs. $R_{C,S} = 0.00354$ in the assimilation step of the final cycle), and in all partial observation cases, QDA achieved a lower RMSE in the final cycle, as further detailed in Table 1. The RMSE results of the vorticity field (Figure 5) showed similar trends, with QDA achieving lower final RMSE values in all cases (Table 1).

In classical 3DVAR single-cycle, the computational complexity of a single assimilation cycle scales as $\mathcal{O}(N^3)$ with respect to the number of grid points N in the assimilated region, due to the matrix operations and inversions. The 3DVAR cost function optimization can be performed using iterative algorithms like the conjugate gradient method, which exhibits $\mathcal{O}(N^2)$ time complexity due to the dense nature of the problem's matrices. In contrast, by reformulating the 3DVAR cost function as an Ising problem and solving it on a quantum device like CIM, significant acceleration can be achieved, as the CIM exhibits linear $\mathcal{O}(N)$ time complexity with respect to the system size. Despite these theoretical advantages, little attention has been paid to how the number of observation points n_{obs} affects assimilation time. We record the computational assimilation

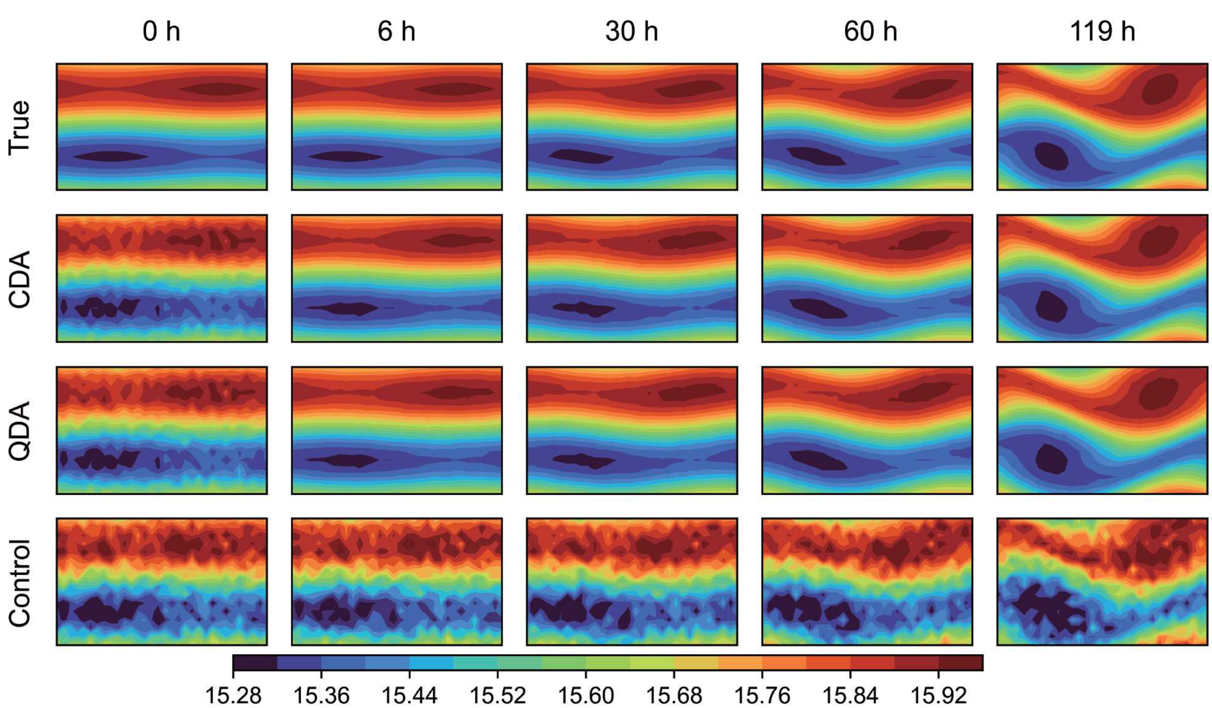

Figure 3 (Color online) Contour plots of the vorticity field over time under full observation conditions. The configuration, including time instances and row arrangement, follows that of Figure 2.

time of each cycle for both stream function and vorticity using CDA and QDA methods, under varying numbers of observation points ($n_{\rm obs}$ = 512, 128, 32, 8). The experimental setup is consistent with that described in Figure 4, and the results are summarized in Table 2. Each reported value represents the average computation time over 120 assimilation cycles. For QDA, the time value reflects the total processing time across six subregions.

As shown in Table 2, QDA's computational time T_Q varies slightly as $n_{\rm obs}$ changes, suggesting its independence from $n_{\rm obs}$. In contrast, CDA shows a significant increase in computational time T_C as $n_{\rm obs}$ increases with $\mathcal{O}\left(N_{\rm obs}^2\right)$ complexity (see Supplementary Material S1). These results highlight the computational advantage of QDA, particularly in scenarios involving dense observational coverage. For instance, under full observation conditions, QDA requires only 15.3% of the time needed by CDA (290 ms vs. 1400 ms). In summary, the numerical simulations demonstrate that QDA offers both improved assimilation accuracy (lower RMSE) and stable computational cost that is independent of the number of observation points. However, the time efficiency advantage still requires experimental validation using physical optical CIM hardware.

3.2 Physical CIM implementation

Figure 6 illustrates the experimental system architecture of a CIM based on a 1550 nm pulsed laser with 1 GHz repetition rate, which solves combinatorial optimization problems through optical parametric oscillation and a closed-loop feedback mechanism. The core of the entire system is a periodically poled lithium niobate (PPLN) crystal. The 1550 nm laser first passes through the initial PPLN crystal for the SHG (second harmonic generation) process, producing a frequency-doubled 775 nm laser. This light serves as the pump light for another PPLN crystal placed within a fiber loop, generating DOPO output pulses of quantum-correlated light. These pulses are measured and controlled through an optical network composed of multiple couplers (Coupler 1-4). Coupler 1 and Coupler 2, located within the loop, function as the beam splitter for DOPO output and the injection beam splitter, respectively. Coupler 3 splits a portion of the fundamental light for injection and measurement, enabling synchronization and dynamic control of the optical field. Coupler 4, together with balanced photodetection, facilitates the experimental measurement of quantum states. The data is then fed back to the control system, forming a closed loop that allows the system to spontaneously evolve toward the

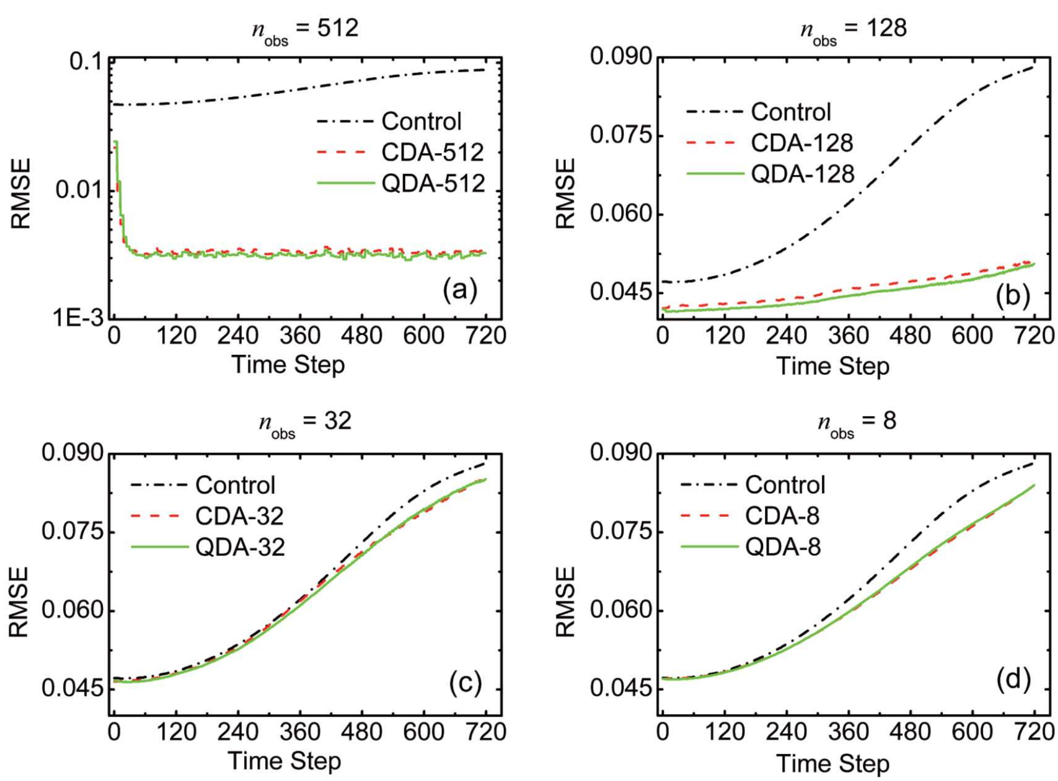

Figure 4 (Color online) RMSE evolution of the stream function field for different numbers of observations. The RMSE is computed to quantitatively evaluate the effectiveness of CDA and QDA assimilation in reducing errors relative to the true field. The control run (black dashed) represents the baseline case without data assimilation, serving as a reference to assess the impact of assimilation. The RMSE for CDA (red), QDA (green), and the control run is plotted for different observation densities: (a) $n_{\rm obs}$ = 512, (b) $n_{\rm obs}$ = 128, (c) $n_{\rm obs}$ = 32, (d) $n_{\rm obs}$ = 8. QDA is implemented using CIM simulator. The comparison highlights how different assimilation strategies and observation densities influence error reduction over time. The percentage values indicate the additional error reduction achieved by QDA compared to CDA in each scenario: (a) 8.8%, (b) 2.7%, (c) 0.6%, (d) 0.07%.

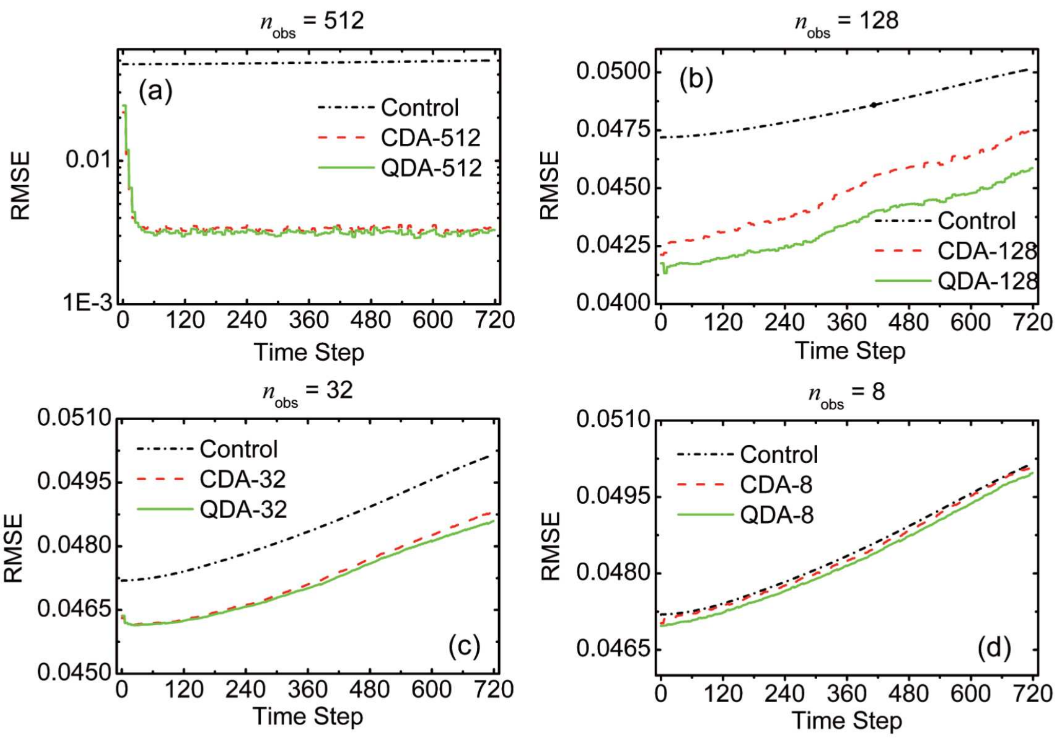

Figure 5 (Color online) RMSE evolution of the vorticity field for different numbers of observations. The setup is identical to Figure 4, except that the assimilated field corresponds to vorticity instead of the stream function. The RMSE for CDA (red), QDA (green), and the control run (black dashed) is plotted for (a) n_{obs} = 512, (b) n_{obs} = 128, (c) n_{obs} = 32, (d) n_{obs} = 8. The percentage values indicate the additional error reduction achieved by QDA compared to CDA in each scenario: (a) 7.1%, (b) 3.6%, (c) 0.5%, (d) 10.2%.

Table 1 RMSE after 120 assimilation cycle under different observation densities (n_{obs}) for CDA and numerically simulated QDA experiments[a)]

n_{obs}	$R_{C,S}$	$R_{Q,S}$	$R_{C,V}$	$R_{Q,S}$
512	0.00354	0.00323	0.00354	0.00329
128	0.05184	0.05043	0.04757	0.04587
32	0.08573	0.08518	0.04882	0.0486
8	0.08404	0.08398	0.05012	0.045

a) Subscripts S and V denote results obtained from separate assimilations of the stream function and the potential vorticity, respectively, using CDA (C) and QDA (Q). Observations are uniformly distributed across the domain: 512 (32×16); 128 (16×8); 32 (8×4); 8 (4×2). RMSE values are computed between the true fields and the forecast fields after 120 assimilation cycles (120 h).

Table 2 Average computational time per assimilation cycle (in ms) for CDA and numerically simulated QDA under different observation densities[a)]

n_{obs}	$T_{C,S}$ (ms)	$T_{Q,S}$ (ms)	$T_{C,V}$ (ms)	$T_{Q,V}$ (ms)
512	1400	290	1393	216
128	266	244	204	215
32	86	246	84	260
8	67	226	67	191

a) Symbols and subscripts follow the same definitions as in Table 1. [2]Reported values represent the average computational time of assimilation step only, over 120 assimilation cycles.

optimal solution. The FPGA module achieves 10-bit coupling resolution capable of processing integer values ranging from −511 to 511. The experimental CIM system is developed by Beijing Qbosen Quantum Technology Co., Ltd.

Figure 7 illustrates the temporal evolution of Ising Hamiltonians for six subtasks using optical CIM devices, each corresponding to distinct subregions of the first stream function assimilation cycle of the total 120 DA cycles, respectively, in the case of n_{obs} = 128. The reason for choosing the example of the stream function with 128 observations and using a real machine to prove time efficiency advantage is that in this simulation scenario, the two computational times $T_{Q,S}$ and $T_{C,S}$ are close (244 ms vs. 266 ms), and the two RMSEs after 120 assimilation cycles are also similar ($R_{Q,S}$ = 0.05043 vs. $R_{C,S}$ = 0.05184).

The precision parameter α of the first stream function assimilation cycle is estimated as $\alpha = \dfrac{\max|Hx_b - y|}{2^Z - 1}$, which is the same in both numerical simulation and optical experiments. The optical pulses encoding the Ising spins were circulated through the fiber loop of the CIM for 2000 round trips to reach the lowest-energy phase configuration and obtain the solution for each subregion DA problem. The computational time is given by $T = T_{rt}\sum_{i=1}^{6} N_i$, where T_{rt}=5.49 μs is the round-trip time and N_i is the number of round-trips for the i-th subregion DA problem shown in Figure 7. The total computation time for six subtasks reached

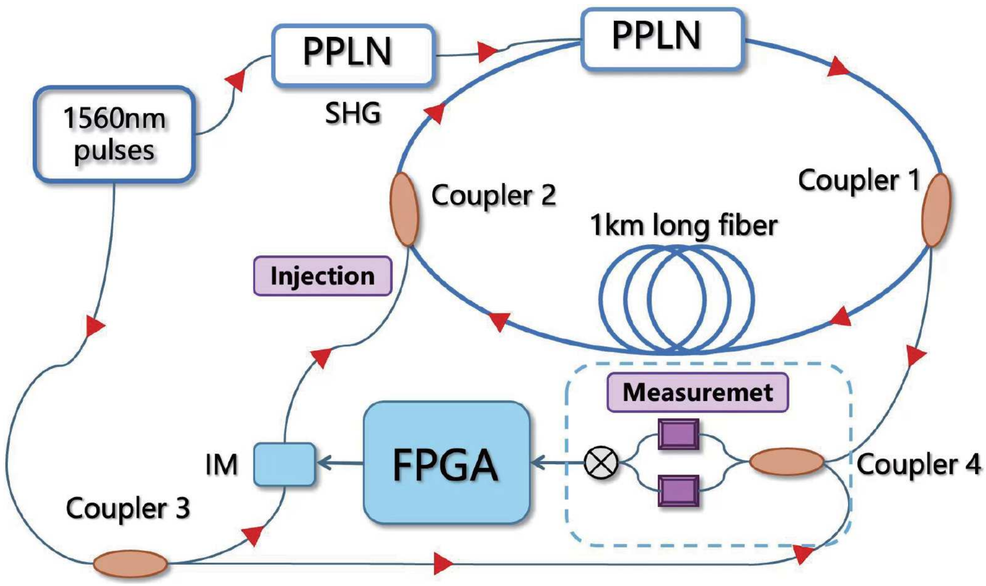

Figure 6 (Color online) Experimental schematic of CIM. The system is a time-division-multiplexed pulsed DOPO implemented in a fiber ring cavity. Nonlinear interactions occur within a PPLN crystal, which serves dual roles: second-harmonic generating (SHG) for optical pumping and facilitating parametric down-conversion with phase-sensitive amplification (PSA) in the fiber ring cavity. A fraction of each pulse is extracted and measured to compute a feedback signal, which is applied via an intensity modulator (IM) and processed by a FPGA. The FPGA stores the quadratic matrix (with 10-bit coupling resolution from −511 to +511) representation of the Ising problem in advance, enabling fast problem-solving.

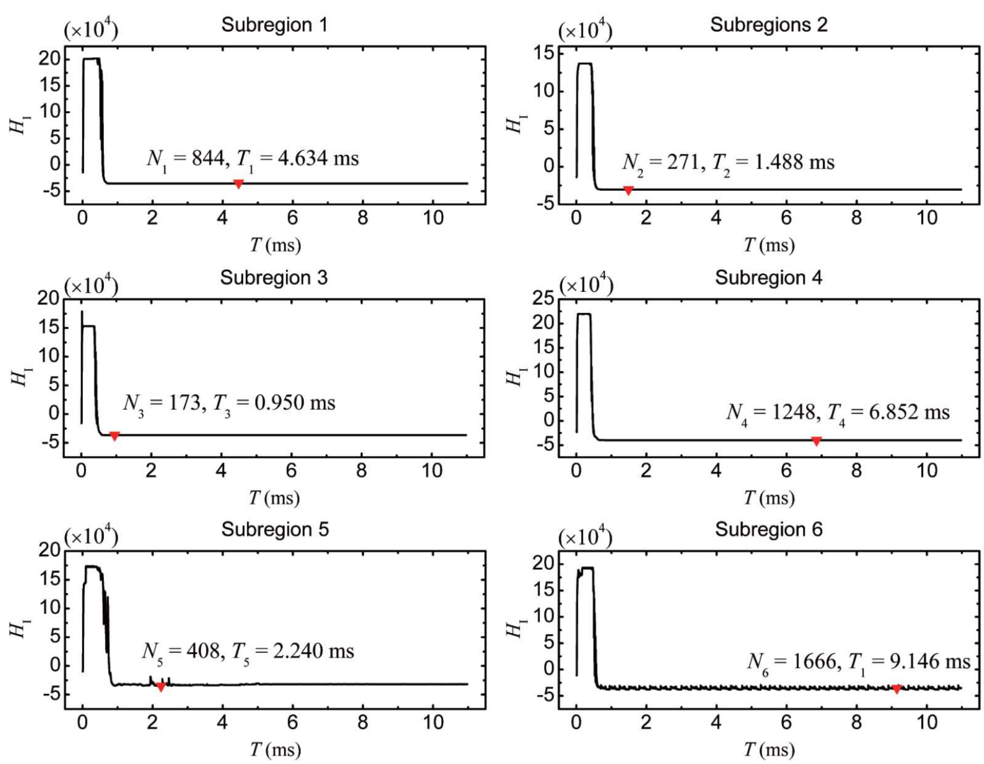

Figure 7 (Color online) Hamiltonian evolution during the solution of subregion Hamiltonian problems using an optical Ising machine for stream function field assimilation with $n_{\mathrm{obs}} = 128$. The 3D-Var cost function is transformed into six overlapping subregion Hamiltonians according to the proposed method and solved using a measurement-feedback DOPO Ising machine in physical experiments. Each plot shows the temporal evolution of the Hamiltonian H_i for a given subregion. Red dots indicate the time T_i at which the minimum Hamiltonian value is reached, along with the corresponding number of iterations N_i; the specific Hamiltonian values are not shown.

25.276 ms. Compared with CDA, the computation time of QDA in the optical CIM experiment is merely 9.5% of CDA's computation time. Table 3 reveals comparable experimental RMSEs despite FPGA precision constraints (10-

Table 3 Subregional RMSEs and computational time for optical CIM-based QDA[a)]

Subregions	$RMSE_{sim}$	$RMSE_{CDA}$	$RMSE_{exp}$	T_{exp} (ms)
1	0.0424	0.04206	0.04607	4.634
2	0.04047	0.04033	0.04331	1.488
3	0.04586	0.04598	0.04578	0.95
4	0.04335	0.04382	0.04412	6.852
5	0.04382	0.0445	0.04761	2.24
6	0.04143	0.04215	0.0418	9.146
Total	0.04194	0.04213	0.04436	25.31

a) The experimental setting corresponds to the case of stream function assimilation with n_{obs}=128 considered in Tables 1 and 2. CIM-based QDA is performed for the first assimilation cycle only. $RMSE_{CDA}$, $RMSE_{sim,}$ and $RMSE_{exp}$ denote the subregional RMSEs obtained from CDA, QDA using a numerical CIM simulator, and QDA implemented on an optical physical CIM, respectively. T_{exp} denotes the computational time for each subregion. For the "Total" row, the RMSE is computed over the reconstructed full domain obtained by merging all subregions, while the corresponding computational time is given by the sum of the subregional times.

bit quantization truncates weak couplings $\left|J_{ij} < 0.5\right|$). Future high-resolution chips could mitigate this limitation. The $RMSE_{exp}$ achieved with the optical CIM experiment is 0.04436 for a 32×16 grid region stream function assimilation. Compared with CDA's RMSE of 0.0421 (0.04194 for simulated QDA), experimental QDA confirms the comparable assimilation quality with greatly reduced computational time.

4 Conclusion

Based on a CIM, we implemented QDA in a 2D quasi-geostrophic model, in which a domain decomposition strategy was employed by dividing the 32×16 grid into 6 overlapping subregions (max dimension: 140 nodes, 1401 Ising variables). After 120 assimilation cycles, the simulated QDA achieved a lower RMSE than the classical 3D-VAR for both the stream function and the vorticity fields. Optical CIM experiments demonstrated the computational efficiency of QDA: single-cycle time T = 25.31 ms (9.5% of classical methods) with comparable accuracy (R_{exp} = 0.04436 vs. R_{CDA} = 0.04213).

By relaxing the RMSE thresholds to 0.0445 (99% energy solutions), the computation time is reduced to less than 5 ms. Current CIM systems support 50000 node computations (8-bit resolution) in T = 22 ms, enabling 55×55 QDA on the grid per cycle. By leveraging the domain decomposition method proposed in this work, our approach allows for data assimilation over significantly larger regions while remaining compatible with existing CIM hardware. Furthermore, our CIM-based QDA exhibits linear time complexity—a critical advantage for high-dimensional applications—while maintaining computational efficiency and accuracy. Future directions include extending to multi-variable applicable atmospheric or oceanic models and leveraging quantum hardware advances for direct high-dimensional optimization. This work demonstrates the potential for quantum computing for time-critical assimilation tasks in environmental forecasting.

This work was supported by the National Natural Science Foundation of China (Grant Nos. 42075011, and 62471058) and the Fund of State Key Laboratory of Information Photonics and Optical Communications, Beijing University of Posts and Telecommunications, China (Grant No. IPOC2022ZT10).

Conflict of interest The authors declare that they have no conflict of interest.

Supporting Information

The supporting information is available online at http://phys.scichina.com and https://link.springer.com. The supporting materials are published as submitted, without typesetting or editing. The responsibility for scientific accuracy and content remains entirely with the authors.

1 R. B. Alley, K. A. Emanuel, and F. Zhang, Science **363**, 342 (2019).
2 P. Bauer, A. Thorpe, and G. Brunet, Nature **525**, 47 (2015).
3 A. Gettelman, A. J. Geer, R. M. Forbes, G. R. Carmichael, G. Feingold, D. J. Posselt, G. L. Stephens, S. C. van den Heever, A. C. Varble, and P. Zuidema, Sci. Adv. **8**, eabn3488 (2022).
4 S. Kotsuki, F. Kawasaki, and M. Ohashi. Nonlin. Processes Geophys. **31**, 237 (2024).
5 C. McGeoch, and P. Farré, *D-Wave Technical Report Series*, Technical Report, (D-Wave Systems Inc., 2022).
6 S. Utsunomiya, K. Takata, and Y. Yamamoto, Opt. Express **19**, 18091 (2011).
7 Z. Wang, A. Marandi, K. Wen, R. L. Byer, and Y. Yamamoto, Phys. Rev. A **88**, 063853 (2013).
8 A. Marandi, Z. Wang, K. Takata, R. L. Byer, and Y. Yamamoto, Nat. Photon. **8**, 937 (2014).
9 T. Inagaki, Y. Haribara, K. Igarashi, T. Sonobe, S. Tamate, T. Honjo, A. Marandi, P. L. McMahon, T. Umeki, K. Enbutsu, et al., Science **354**, 603 (2016).
10 T. Honjo, T. Sonobe, K. Inaba, T. Inagaki, T. Ikuta, Y. Yamada, T. Kazama, K. Enbutsu, T. Umeki, R. Kasahara, et al., Sci. Adv. **7**, eabh0952 (2021).
11 Q. Cen, H. Ding, T. Hao, S. Guan, Z. Qin, J. Lyu, W. Li, N. Zhu, K. Xu, Y. Dai, et al., Light Sci. Appl. **11**, 333 (2022).
12 E. Ising, Z. Phys. **31**, 253 (1925).
13 H. Takesue, K. Inaba, T. Honjo, Y. Yamada, T. Ikuta, Y. Yonezu, T. Inagaki, T. Umeki, and R. Kasahara, Sci. Adv. **11**, eads7223 (2025).
14 A. Farghadan, M. M. Masteri Farahani, and M. Akbari, Sci. Rep. **15**, 5317 (2025).
15 S. Yarkoni, E. Raponi, T. Bäck, and S. Schmitt, Rep. Prog. Phys. **85**, 104001 (2022).
16 Y. Yamamoto, K. Aihara, T. Leleu, K. Kawarabayashi, S. Kako, M. Fejer, K. Inoue, and H. Takesue, npj Quantum Inf. **3**, 49 (2017).
17 M. Mu, and Z. Zhang, J. Atmos. Sci. **63**, 1587 (2006).
18 W. R. Holland, J. Phys. Oceanogr. **8**, 363 (1978).
19 J. D. McCalpin, and D. B. Haidvogel, J. Phys. Oceanogr. **26**, 739 (1996).
20 G. Evensen, J. Geophys. Res. **97**, 17905 (1992).
21 G. Evensen, J. Geophys. Res. **99**, 10143 (1994).
22 C. Cotter, D. Crisan, D. Holm, W. Pan, and I. Shevchenko, J. Stat. Phys. **179**, 1186 (2020).
23 B. Buongiorno Nardelli, Earth Syst. Sci. Data **12**, 1711 (2020).

24 M. Mu, and T. G. Shepherd, Geophys. Astrophys. Fluid Dyn. **75**, 21 (1994).
25 W. Lenz, Z. Phys. **21**, 613 (1920).
26 Z. Wang, *Coherent Computation in Degenerate Optical Parametric Oscillators*, Dissertation for the Doctoral Degree, (Stanford University, Stanford, 2015).
27 F. Bouttier, and P. Courtier, *Meteorological Training Course Lecture Series*, Education Material, (ECMWF, 2002).
28 S. E. Ahmed, S. Pawar, and O. San, Fluids **5**, 225 (2020).
29 Z. Zhou, Y. Du, X. Tian, and D. Tao, Phys. Rev. Appl. **19**, 024027 (2023).
30 Z. Li, Y. Chao, J. C. McWilliams, and K. Ide, J. Atmos. Ocean. Tech. **25**, 2074 (2008).
31 A. Arakawa, J. Comput. Phys. **135**, 103 (1997).
32 O. Caumont, V. Ducrocq, É. Wattrelot, G. Jaubert, and S. Pradier-Vabre, Tellus A-Dyn. Meteor. Oceanogr. **62**, 173 (2010).
33 S. Ballard, Z. Li, D. Simonin, H. Buttery, C. Charlton-Perez, N. Gaussiat, and L. Hawkness-Smith, IAHS-AISH Publ. **351,** 336 (2012).
34 H. Wang, J. Sun, S. Fan, and X. Y. Huang, J. Appl. Meteor. Climatol. **52**, 889 (2013).
35 K. Stephan, S. Klink, and C. Schraff, Quart. J. R. Meteor. Soc. **134**, 1315 (2008).